

Nuclear heating and melted layers in the inner crust of an accreting neutron star

Edward F. Brown¹

Department of Physics and Department of Astronomy

601 Campbell Hall # 3411, University of California, Berkeley, CA 94720-3411

`brown@oddjob.uchicago.edu`

ABSTRACT

A neutron star in a long-lived, low-mass binary can easily accrete enough matter to replace its entire crust. Previous authors noted that an accreted crust, being formed from the burning of accreted hydrogen and helium, allows a series of non-equilibrium reactions, at densities $\gtrsim 6 \times 10^{11} \text{ g cm}^{-3}$, which release a substantial amount of heat ($\sim 1 \text{ MeV}$ per accreted nucleon). Recent calculations by Schatz et al. showed that the crystalline lattice of an accreted crust is also likely to be quite impure. This paper discusses the thermal structure of such a neutron star and surveys how the crust reactions and impurities affect the crust temperature. During accretion rapid enough to make the accreted hydrogen and helium burn stably ($\dot{M} \sim 10^{-8} M_{\odot} \text{ yr}^{-1}$; typical of the brightest low-mass neutron star binaries), most of the heat released in the crust is conducted into the core, where neutrino emission regulates the temperature. As a result there is an inversion of the thermal gradient: the temperature decreases with depth in the inner crust. The thermal structure in the crust at these high accretion rates is insensitive to the temperature in the hydrogen/helium burning shell. When the crust is very impure, the temperature can reach $\approx 8 \times 10^8 \text{ K}$ at densities $\gtrsim 6 \times 10^{11} \text{ g cm}^{-3}$. This peak temperature depends mostly on the amount of heat released and the thermal conductivity and in particular is roughly independent of the core temperature. The high crust temperatures are sufficient to melt the crystalline lattice in thin layers where electron captures have substantially reduced the nuclear charge.

Subject headings: accretion, accretion disks — conduction — stars: neutron — stars: interiors

¹Current Address: University of Chicago, Astronomy and Astrophysics, 5640 S Ellis Ave, Chicago, IL 60637; `brown@oddjob.uchicago.edu`

1. Introduction

Many of the known neutron stars reside in low-mass x-ray binaries. These sources typically accrete at rates of $10^{-11} M_{\odot} \text{ yr}^{-1}$ to $10^{-8} M_{\odot} \text{ yr}^{-1}$ and show no conclusive evidence, such as cyclotron lines or coherent pulsations (in the persistent emission), of a magnetic field. In contrast to studies of isolated neutron star cooling (for a review, see Tsuruta 1998), there has been much less interest in the interior thermal state of an accreting neutron star. Originally, studies of how accretion affected a neutron star’s thermal structures were motivated by the challenge of explaining the type I x-ray bursts of some of these sources. Both Lamb & Lamb (1978) and Ayasli & Joss (1982) estimated the steady-state core temperature by balancing the heating from hydrogen and helium shell burning with neutrino and radiative losses. Later, Fujimoto et al. (1984) and Hanawa & Fujimoto (1984) calculated the thermal evolution of the entire neutron star, both for steady hydrogen and helium burning (Fujimoto et al. 1984) and for repeated shell flashes (Hanawa & Fujimoto 1984). In all of these works, the only heat sources considered were the hydrogen/helium burning and the influx of entropy by the accreted matter. Both Fujimoto et al. (1984) and Hanawa & Fujimoto (1984), who considered accretion rates $\lesssim 5 \times 10^{-9} M_{\odot} \text{ yr}^{-1}$, found that the deep crust and core would gradually become isothermal, at a temperature $\gtrsim 10^8$ K, if there were no enhanced neutrino cooling; otherwise, the core would remain chilled at temperatures $\sim 10^7$ K. Without heat sources in the crust, the temperature of the deep crust tracks that of the core and is therefore sensitive to the cooling from neutrino processes active in the core.

Unlike an isolated neutron star, the crust of an accreting neutron star is not in statistical nuclear equilibrium, but rather has a composition set by the nuclear history of the accreted material (Sato 1979; Blaes et al. 1990, 1992; Haensel & Zdunik 1990a,b). The atmosphere is composed of the accreted helium and hydrogen and any metals present (see Bildsten, Salpeter, & Wasserman 1992 for a discussion). This accumulated fuel eventually burns to heavier elements. The accretion of fresh fuel shoves the original crust deeper and, if continued over a long enough interval, will eventually replace the original crust with one formed by the ashes of hydrogen/helium burning. Compression of the crust by the weight of continually accreting material induces non-equilibrium reactions that release heat.

The composition of the replaced crust is uncertain. Improved treatments of the physics of hydrogen and helium nuclear burning revealed that the ashes of this burning are unlikely to be a pure species, e.g., iron. The mixture is formed by the rp-process (Wallace & Woosley 1981; Champagne & Wiescher 1992; Van Wormer et al. 1994; Schatz et al. 1998), a sequence of rapid proton captures onto seed nuclei provided by helium and CNO burning. Calculations of the nucleosynthetic yield from the rp-process have been done, both for unstable burning during an x-ray burst (Koike et al. 1999) and for steady-state hydrogen and helium burning (Schatz et al. 1999). The ashes of the stable burning are a motley mix of iron-peak elements, so that the crust formed from these ashes will likely be very impure (Schatz et al. 1999).

This paper studies the crustal temperatures of steadily accreting neutron stars with low mag-

netic fields. There are two differences with Miralda-Escudé, Paczynski, & Haensel (1990) and Zdunik et al. (1992), both of which included crust reactions in the neutron star’s thermal balance. First, this work considers the stable regime of hydrogen/helium burning, which requires rapid accretion (near the Eddington limit, $\sim 10^{-8} M_{\odot} \text{yr}^{-1}$). At the low accretion rates ($\dot{M} \lesssim 10^{-10} M_{\odot} \text{yr}^{-1}$, roughly two orders of magnitude less than the Eddington limit) considered by Miralda-Escudé et al. (1990) and Zdunik et al. (1992), the crust is basically isothermal, with a temperature locked to that of the core. Second, this work allows for an impure crust by surveying both high- and low-conductivity cases. Previous calculations have assumed the impurity concentration to be much less than unity.

At the rapid accretion rates considered here, the neutrino luminosity from modified Urca processes and crust bremsstrahlung is significant and causes the temperature to decrease with depth in the inner crust (Brown & Bildsten 1998). Almost all of the heat produced in the crust flows inward. Moreover, the reduced conductivity of the impure crust produces a peaked thermal profile with a maximum temperature where the nuclear reactions heat the crust, at densities $\gtrsim 6 \times 10^{11} \text{g cm}^{-3}$. The thermal profile in the crust is primarily determined by the ability of the inner crust to conduct a flux of $\sim 1 \text{MeV}$ per accreted baryon into the core, and is insensitive to the temperature of the hydrogen/helium burning shells. If the crust is very impure, the crust reaches temperatures $\approx 8 \times 10^8 \text{K}$; the value of this temperature only weakly depends on the core temperature.

Electron captures in the crust reduce the charge of the nuclei (Z) and hence the electrostatic binding of the lattice. For the hottest temperatures in the crust, this low- Z lattice melts where the charge is lowest ($Z \lesssim 15$ for the composition of Haensel & Zdunik 1990a). As a result, the inner crust of the neutron star comes to resemble a “layer cake,” with alternating layers of lattice and liquid.

This paper is relevant for the brightest low-mass x-ray binaries. These weakly magnetized neutron stars are considered possible progenitors of millisecond pulsars (for a review, see Bhattacharya 1995), and there has been much theoretical interest in the evolution of the crust magnetic field (Romani 1990; Geppert & Urpin 1994; Urpin & Geppert 1995; Konar & Bhattacharya 1997; Brown & Bildsten 1998; Urpin, Geppert, & Kononov 1998). Many of these neutron stars rotate within an apparently narrow range of spin frequencies $\sim 300 \text{Hz}$ (van der Klis 1998, e.g.). One possibility for this convergence of spin frequencies is that gravitational radiation from the neutron star balances the accretion torque (Bildsten 1998; Andersson et al. 1999). The source for the gravitational radiation could be a mass quadrupole formed by misaligned electron capture layers in the crust (Bildsten 1998) or a current quadrupole from an r-mode instability in the core (Andersson 1998; Friedman & Morsink 1998; Lindblom, Owen, & Morsink 1998; Owen et al. 1998; Andersson, Kokkotas, & Schutz 1999; Andersson, Kokkotas, & Stergioulas 1999). All of these problems depend on the thermodynamics of the neutron star’s crust and core and motivate this paper.

1.1. An overview of the problem

A neutron star has several distinctive regions. The *core* consists of uniform npe^- (in the least dense parts). At a baryon density less than $n \approx 0.6n_s$, where $n_s = 0.16 \text{ fm}^{-3}$ is the saturation density² of nuclear matter, individual nuclei appear (Pethick, Ravenhall, & Lorenz 1995). The portion of the neutron star exterior to this point, the *inner crust*, is composed of nuclei, degenerate neutrons, and relativistic degenerate electrons. Where the electron Fermi energy is less than about twice the nuclear bulk energy ($\approx 30 \text{ MeV}$; see Pethick & Ravenhall 1998), free neutrons can no longer exist in β -equilibrium. This point, *neutron drip*, has a density $\approx 0.0023n_s$ ($4 \times 10^{-4} \text{ fm}^{-3}$) and marks the boundary between the inner and the *outer crust*. At lesser densities, the crust is made of nuclei and electrons, with the degenerate electrons supplying the pressure. The outer and inner crust collectively occupy the outermost kilometer or so of the neutron star and contain a total mass of order $0.01M_\odot$.

The boundaries of the crust are demarcated by surfaces of constant pressure. For a thin crust, the mass above a given isobar is fixed by the surface gravity and area. As a consequence, accretion during a time brief compared with M/\dot{M} (so that the overall structure of the neutron star remains roughly constant) pushes the underlying crust through these compositional boundaries. Low-mass x-ray binaries live for more than 10^8 yr (Webbink, Rappaport, & Savonije 1983); even at $\dot{M} = 10^{-10} M_\odot \text{ yr}^{-1}$, the neutron star can easily accrete enough material from the secondary to replace its entire crust. This replaced crust is composed of the ashes of hydrogen and helium burning and is quite different in composition from the original. Unlike during the neutron star’s hot birth, the crust does not burn to nuclear statistical equilibrium. As the ashes of the hydrogen and helium burning are pushed deeper into the crust, the rising electron Fermi energy induces a series of electron captures (Haensel & Zdunik 1990b; Sato 1979; Blaes et al. 1990). Further compression of this low- Z material causes neutron emissions and pycnonuclear reactions (Haensel & Zdunik 1990b; Sato 1979). A schematic of the composition, from the calculation of Haensel & Zdunik (1990b), is shown in Figure 1. Each decrease in the nuclear charge Z (*bottom panel*) is from an electron capture, and each decrease in the nuclear mass number A (*top panel*) is from a neutron emission. Where a pycnonuclear reaction occurs, both Z and A double.

The pycnonuclear reactions and neutron emissions liberate $E_N \approx 1 \text{ MeV}$ for each baryon accreted and heat the crust at a rate $L_N \approx 10^{36} (\dot{M}/10^{-8} M_\odot \text{ yr}^{-1}) \text{ erg s}^{-1}$. To set the scale for the core temperature, note that the core must be at a temperature $\approx 4 \times 10^8 (L_N/10^{36} \text{ erg s}^{-1})^{1/8} \text{ K}$ for modified Urca processes (Friman & Maxwell 1979; Yakovlev & Levenfish 1995) to radiate a neutrino luminosity equal to L_N . If the nucleons in the core were superfluid and the modified Urca processes correspondingly suppressed, crust neutrino bremsstrahlung (Maxwell 1979; Yakovlev & Kaminker 1996; Haensel, Kaminker, & Yakovlev 1996; Itoh et al. 1996) can also balance L_N for an

²Density is measured in units of fm^{-3} and pressure in units of MeV fm^{-3} . Note that throughout the crust, $\rho \approx nm_u = 1.66 \times 10^{14} (n/0.1 \text{ fm}^{-3}) \text{ g cm}^{-3}$, where $m_u = 1.66 \times 10^{-24} \text{ g}$ is the atomic mass unit, and $1 \text{ MeV fm}^{-3} = 1.6 \times 10^{33} \text{ dyne cm}^{-2}$.

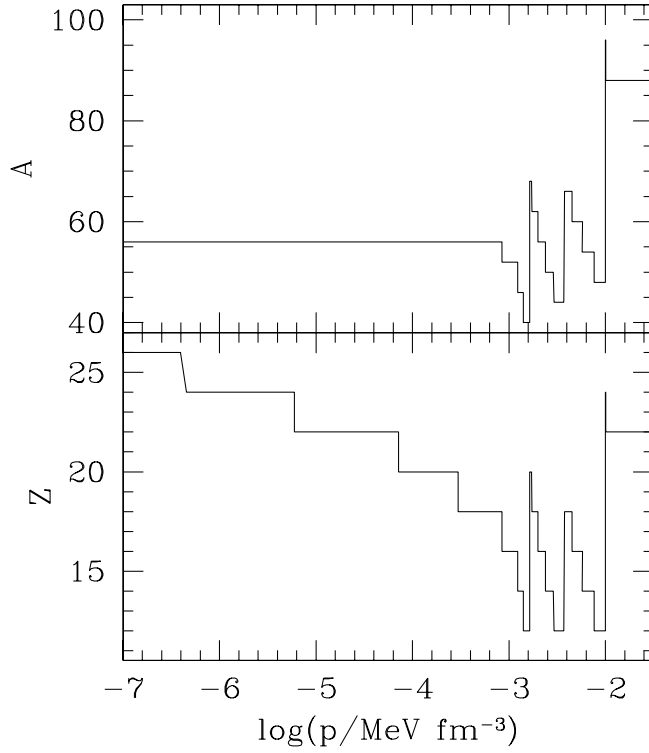


Fig. 1.— Composition of an accreted crust, as computed by Haensel & Zdunik (1990b). Shown are the mass number (*top panel*) and charge number (*bottom panel*) as a function of pressure. The mass resting above a given isobar is given by equation (8). Electron captures produce a downward jump in Z ; neutron emissions produce a downward jump in A . The upward jumps in both Z and A indicate a pycnonuclear reaction.

inner crust temperature $\approx 6 \times 10^8 (L_N/10^{36} \text{ erg s}^{-1})^{1/6} \text{ K}$.

The luminosity from the steady-state hydrogen/helium burning ($\approx 5 \text{ MeV}$ per accreted baryon; Schatz et al. 1999) is much larger than that flowing out from deeper in the crust. As a result, the temperature at the base of the hydrogen/helium burning shell is determined by the luminosity there (for a review, see Bildsten 1998) and is $\approx 5 \times 10^8 \text{ K}$ for $\dot{M} \approx 10^{-8} M_\odot \text{ yr}^{-1}$ (Brown & Bildsten 1998; Schatz et al. 1999). The conductivity is much greater in the inner crust (the conductivity in the crust increases with density), while the thickness of the inner crust is only a factor of two greater than the thickness of the outer crust. For a similar thermal gradient, the inner crust can carry a much larger flux. If the change in temperature between the hydrogen/helium burning shell and neutron drip is of the same order as the change in the inner crust, than most of the nuclear luminosity generated in the crust will flow into the core (Brown & Bildsten 1998).

1.2. Outline of this paper

The remainder of this paper paints in the crude picture just sketched. Sections 2 and 3 develop the details of the calculation, which proceeds in two steps. First, the hydrostatic structure of the neutron star is computed for different equations of state (§ 2.1) and neutron star masses. These hydrostatic models serve as background for the thermal computations, which are discussed in § 3. Section 3 also describes the relevant microphysics: the heating by crust reactions and the cooling by the crust and core neutrino emissivity (§ 3.1); the reduction of the core neutrino emissivity by neutron and proton superfluidity (§ 3.2); and the conductivity of the crust and core (§ 3.3), including the effect of impurities.

Section 4 contains the results of these calculations, which are split into three parts. First, there is discussion on the nature of the thermal profile and its dependence on the crust composition and the core neutrino emissivity (§ 4.1). Section 4.2 presents some analytical formulae for the crust temperature; these formula are used (§ 4.3) to show how the high-accretion rate solutions discussed here connect with those at lower accretion rates (e.g., Miralda-Escudé et al. 1990; Zdunik et al. 1992). The melting and refreezing of the crystalline lattice in the inner crust are discussed in § 4.4.

2. Hydrostatic structure

Throughout the crust and core, the pressure is supplied by degenerate particles with Fermi energies $\gg k_B T$, and so the equation of state (EOS) scarcely depends on temperature. The crust reactions heat the core on a timescale

$$\tau_H \sim \left(\frac{M}{m_u} \right) \frac{CT}{L_N} \approx \frac{M CT}{\dot{M} E_N} \ll \frac{M}{\dot{M}}. \quad (1)$$

In this equation C is the specific heat per baryon, M/m_n is approximately the number of baryons in the star, and M/\dot{M} is the timescale for the mass to increase from accretion. If the heat is stored

in the electrons (as would be the case if the neutrons were superfluid), the heat content per baryon (e.g., Landau & Lifshitz 1980) is $CT \approx \pi^2 k_B T (k_B T / E_{F,e}) \ll E_N$, where $E_{F,e}$ is the electron Fermi energy. The heat content per baryon is similar if the neutrons are normal (Lamb & Lamb 1978). Equation (1) shows that over timescales necessary to establish a thermal steady-state, the mass of the star changes only slightly, and so the hydrostatic equations need not be solved simultaneously with the thermal equations. Using a fixed hydrostatic structure simplifies the thermal calculation.

To calculate the temperature as a function of radius requires integrating the heat transport equations over the star. The strong gravitational field modifies the heat flow. In an isothermal star, where there is no heat flow, the *redshifted* temperature is constant, while the proper (as measured by a local thermometer) temperature increases as one moves toward the stellar center. Because the neutrino emissivity is a strong function of temperature, the thermal transport equations must account for gravitational effects. The appropriate equations, solved for stellar mass and EOS, are the post-Newtonian stellar structure equations (Thorne 1977) for the radius, gravitational mass, potential, and pressure:

$$\frac{\partial r}{\partial a} = (4\pi r^2 n)^{-1} \left(1 - \frac{2Gm}{rc^2}\right)^{1/2} \quad (2)$$

$$\frac{\partial m}{\partial a} = \frac{\rho}{n} \left(1 - \frac{2Gm}{rc^2}\right)^{1/2} \quad (3)$$

$$\frac{\partial \Phi}{\partial a} = \frac{Gm}{4\pi r^4 n} \left(1 + \frac{4\pi r^3 p}{mc^2}\right) \left(1 - \frac{2Gm}{rc^2}\right)^{-1/2} \quad (4)$$

$$\frac{\partial p}{\partial a} = -\frac{Gm}{4\pi r^4} \frac{\rho}{n} \left(1 + \frac{p}{\rho c^2}\right) \left(1 + \frac{4\pi r^3 p}{mc^2}\right) \left(1 - \frac{2Gm}{rc^2}\right)^{-1/2}. \quad (5)$$

In these equations the Lagrangian variable a is the total number of baryons inside a sphere of area $4\pi r^2$, and ρ is the mass density. The potential Φ appears in the time-time component of the metric as e^{Φ/c^2} (it governs the redshift of photons and neutrinos; Misner, Thorne, & Wheeler 1973) and satisfies the boundary condition that at the stellar surface $e^{2\Phi/c^2}|_{r=R} = 1 - 2GM/Rc^2$, where \mathcal{M} and $4\pi R^2$ are the total gravitational mass and surface area of the neutron star.

2.1. Equation of state

For purposes of calculating the crust EOS, the ashes of hydrogen and helium burning are presumed to be pure iron (but see the discussion in § 3.3 on how the composition affects the energy release and heat transport). As a mass element is compressed to greater densities and pressures, the rising electron Fermi energy triggers a series of electron captures, neutron emissions, and pycnonuclear reactions (Sato 1979; Blaes et al. 1990; Haensel & Zdunik 1990b). At any given density, only one species is assumed present (see Figure 1) according to the composition calculated by Haensel & Zdunik (1990a,b).

In the outer crust, relativistic degenerate electrons of density $n_e = Y_e n$ supply the pressure. The electron chemical potential is basically the Fermi energy $E_{F,e} = m_e c^2 [1 + (3\pi^2 n_e)^{2/3} \lambda_e^2]^{1/2}$, where $\lambda_e = 386.2 \text{ fm}$ is the electron Compton wavelength. I calculate the electron pressure, which is approximately $n_e E_{F,e}/4$, from the interpolation formula of Paczyński (1983). The lattice pressure is calculated from the ionic free energy, which is a function of

$$\Gamma = \frac{Z^2 e^2}{k_B T} \left(\frac{4\pi}{3} n_N \right)^{1/3}, \quad (6)$$

where n_N is the density of nuclei. I use the fits of Farouki & Hamaguchi (1993) to Monte-Carlo simulations of the free energy. (In the crust, the free energy per nucleus is to lowest order just the Madelung energy, $\approx -0.9\Gamma k_B T$.) These fits are valid for $\Gamma > 1$, which is always the case for the density-temperature regime of interest. Following Farouki & Hamaguchi (1993), I presume the nuclei are crystalline for $\Gamma \geq 173$. The binding energy of the nuclei are computed from a compressible liquid-drop model (Mackie & Baym 1977). This formula accounts for an external neutron gas and is therefore applicable at densities greater than neutron drip. The energy density and pressure of the neutron gas (which differ from that of an ideal degenerate gas) are also computed with this model in the limit of a vanishing proton fraction.

Summing the pressure contributions from electrons, ions, and neutrons gives the crust EOS, which agrees with that of Haensel & Zdunik (1990a) to the accuracy of their table. Figure 2 displays this relation, $p(n)$, throughout the inner crust. For reference, the $p \propto n^{4/3}$ relation appropriate for an EOS dominated by relativistic, degenerate electrons is also shown (*dotted line*). Free neutrons are present (*heavy solid line*) for $n > 3.6 \times 10^{-4} \text{ fm}^{-3}$. As noted by Haensel & Zdunik (1990a), for $n > 0.04 \text{ fm}^{-3}$, the free neutrons provide most of the pressure, and the ionic composition becomes less and less important to the EOS. In this regime I use the $p(n)$ fit of Negele & Vautherin (1973).

At $n \gtrsim 0.1 \text{ fm}^{-3}$, the nuclei dissolve into uniform nuclear matter (Pethick et al. 1995). I select two sample core equations of state for comparison. The first EOS is a fit (Lai 1994) to the AV14+UVII interaction, which is the Argonne V14 potential, with a three-nucleon interaction prescribed by the Urbana VII potential (Wiringa, Fiks, & Fabrocini 1988). The second EOS, called AV18+ δv +UIX*, is a Skyrme-type Hamiltonian fit (Akmal, Pandharipande, & Ravenhall 1998, appendix A) to the Argonne V18 potential, with relativistic boost corrections and the three-nucleon interaction UIX* (Akmal et al. 1998). The components of both interactions are neutrons, protons, electrons, and, where $E_{F,e} > m_\mu c^2 = 105.66 \text{ MeV}$, muons. I do not consider, for simplicity, other possible components (e.g., hyperons or quark matter) in the EOS. To construct a table suitable for interpolating $n(p)$, I calculate for each n the proton fraction $Y_p = n_p/n$ and electron fraction $Y_e = n_e/n$ from the equations for β -equilibrium, $\mu_n - \mu_p = \mu_e = \mu_\mu$, and charge neutrality, $n_p = n_e + n_\mu$. Given (Y_p, Y_e) , I then compute the mass density ρ and pressure $p = c^2(-\rho + n\partial\rho/\partial n)$.

There have been many attempts to calculate the density of the phase transition from the inner crust to the core (see Pethick & Ravenhall 1995, and references therein). I adopt the following approach. The density and pressure of the AV18+ δv +UIX* EOS equal those of Negele & Vautherin

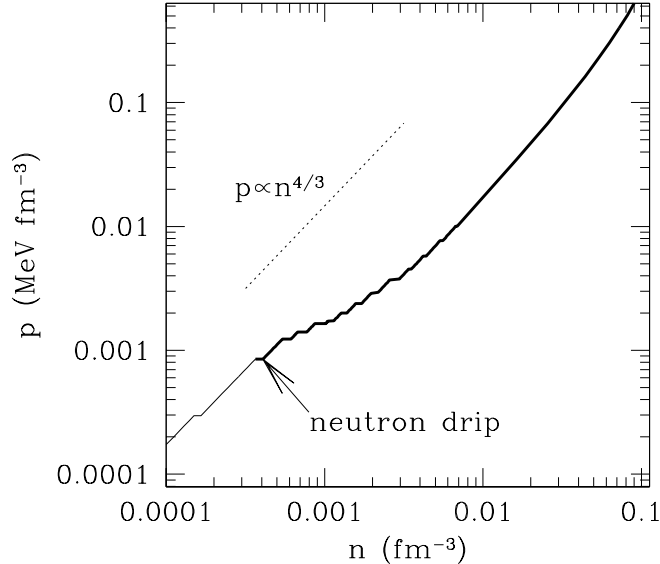


Fig. 2.— Pressure as a function of baryon density n in the crust. Each electron capture is visible as a discontinuity in n . Where free neutrons are present (*heavy solid line*) the pressure deviates from the piecewise scaling for degenerate, relativistic electrons (*dotted line*).

(1973) at $n = 0.078 \text{ fm}^{-3}$, $p = 0.39 \text{ MeV fm}^{-3}$. I therefore take this density as the transition from crust to core; there is no density discontinuity in this case. For the AV14+UVII EOS, the energy density is always greater than that of Negele & Vautherin (1973), and so I choose the maximum crust density to be 0.1 fm^{-3} ($p = 0.60 \text{ MeV fm}^{-3}$). In this case, there is a substantial density jump (from $n = 0.1 \text{ fm}^{-3}$ to $n = 0.13 \text{ fm}^{-3}$) between crust and core. The choice $n = 0.1 \text{ fm}^{-3}$ as the upper limit for the crust density reflects recent detailed calculations (Pethick et al. 1995) of the phase transition.

For equilibrium crust compositions, it becomes energetically favorable for nuclei to turn inside-out in the inner crust and form a phase with bubbles of neutron gas encased in bound nuclear matter (Lorenz, Ravenhall, & Pethick 1993; Oyamatsu 1993). Because the charge of nuclei in an accreted crust is less than that of the equilibrium composition, it is possible that the nuclei do not turn inside-out. The condition for this inversion (see, e.g., Pethick & Ravenhall 1995) is that the nuclear radius be more than one-half the Wigner-Seitz radius, $(4\pi n_N/3)^{-1/3}$. For the core EOS AV18+ δv +UIX*, this ratio at the bottom of the crust is (for $Z = 20$, $A = 100$, $Y_n = 0.8$, where $Y_n = n_n/n$ is the neutron fraction) 0.50. For the core EOS AV14+UVII, the ratio is 0.54. In the absence of a more detailed calculation of the composition, I am unable to say if an accreted crust contains non-spherical nuclei and have not explored this possibility.

2.2. Construction of models

With $n(p)$ specified by interpolation from a table, I integrate equations (2)–(5) with a fourth-order Runge-Kutta integration algorithm (Press et al. 1992). Borrowing a technique used by van Riper (1991), the code restricts the stepsize Δa to be always less than some fraction f of the reciprocal sum of the radial and baric scale heights,

$$\Delta a \leq f \left(\frac{\partial \ln r}{\partial a} - \frac{\partial \ln P}{\partial a} \right)^{-1}. \quad (7)$$

Starting from a fixed central pressure, I expand the hydrostatic equations about the center $a = m = r = 0$ and integrate outwards until the pressure is less than $3.4 \times 10^{-8} \text{ MeV fm}^{-3}$ (corresponding to a density $n \approx 2.4 \times 10^{-8} \text{ fm}^{-3}$, about a factor of 10 greater than where the helium burning ends; Schatz et al. 1999). At this pressure, the radius and mass are constant to within $10^{-5} R$ and $10^{-9} M$, respectively. The algorithm iteratively adjusts the central pressure until a target gravitational mass \mathcal{M} is reached. The integration steps are then stored for later use in solving the thermal equations. For each of the two equations of state, AV14+UVII and AV18+ δv +UIX*, I compute two masses, $\mathcal{M} = 1.4M_{\odot}$ and $\mathcal{M} = 1.8M_{\odot}$; a summary of these four structures is provided in Table 1.

Despite continuous accretion, the pressure is a good Eulerian coordinate throughout the crust (Bildsten et al. 1992; Brown & Bildsten 1998), and I shall plot the temperature and luminosity against it. The mass contained in the crust above a given isobar is to lowest order (from expanding eq. [5]; Lorenz et al. 1993)

$$\begin{aligned} \Delta M &= m_n \Delta a \approx \frac{p}{g} 4\pi R^2 \\ &= 0.05M_{\odot} \left(\frac{p}{\text{MeV fm}^{-3}} \right) \left(\frac{R}{10 \text{ km}} \right)^2 \left(\frac{2 \times 10^{14} \text{ cm s}^{-2}}{g} \right), \end{aligned} \quad (8)$$

where $g = GM(1+z)/R^2$ is the gravitational acceleration and $(1+z) = (1 - 2GM/Rc^2)^{-1/2}$ is the surface redshift. Table 1 lists ΔM , g , and $1+z$ for the two masses and two EOSs considered in this paper.

3. Thermal Structure

With a hydrostatic structure specified, the luminosity L and temperature T are found by solving the entropy and flux equations (Thorne 1977),

$$e^{-2\Phi/c^2} \frac{\partial}{\partial r} \left(L e^{2\Phi/c^2} \right) - 4\pi r^2 n (\epsilon_N - \epsilon_{\nu}) (1 - 2Gm/rc^2)^{-1/2} = 0 \quad (9)$$

$$e^{-\Phi/c^2} K \frac{\partial}{\partial r} \left(T e^{\Phi/c^2} \right) + \frac{L}{4\pi r^2} (1 - 2Gm/rc^2)^{-1/2} = 0. \quad (10)$$

Here ϵ_N and ϵ_{ν} are the nuclear heating and neutrino emissivity per baryon, and K is the thermal conductivity. I neglect in equation (9) terms arising from compressional heating, as they are of

order $T\Delta s(\dot{M}/M)$ (Fujimoto & Sugimoto 1982), s being the specific entropy, and are negligible throughout the degenerate crust and core (Brown & Bildsten 1998). The physics of the problem is contained in the heating ϵ_N , neutrino cooling ϵ_ν , and the conductivity K ; the following sections discuss each in turn.

3.1. Nuclear heating and neutrino cooling

As mentioned in § 2.1, the crust electron captures reduce the charge of the nuclei enough to trigger pycnonuclear reactions. The rate of pycnonuclear reactions is governed by the supply of low- Z nuclei, which is in turn determined by the rate of the preceding electron capture. As a result, even though the pycnonuclear reactions are better described at typical crust temperatures as strongly screened fusion reactions (Salpeter & van Horn 1969), they are insensitive to temperature and hence not susceptible to a thermal instability.

To find the overall thermal profile, I do not need to resolve the individual capture layers. Rather, I distribute the reaction heat per baryon, $E_N = 1$ MeV, over a pressure interval Δp between 8.7×10^{-4} MeV fm $^{-3}$ and 3.4×10^{-2} MeV fm $^{-3}$ (this covers the region where the pycnonuclear reactions occur). The total nuclear luminosity is $L_N = \dot{M}e^{-\Phi}E_N/m_n \approx L_A/200$, where $L_A = \dot{M}c^2z/(1+z) \approx G\dot{M}M/R$ is the accretion luminosity (see § 3.4) and $\dot{M}e^{-\Phi}$ is the accretion rate as measured in the crust. The heating term in equation (9) is therefore

$$4\pi r^2 n \epsilon_N = \left(\frac{E_N}{m_n} \dot{M} e^{-\Phi/c^2} \right) \left(\frac{1}{\Delta p} \frac{\partial p}{\partial r} \right), \quad (11)$$

where $\partial p/\partial r$ is the Jacobean.

The cooling terms in equation (9) are evaluated from various fits to microscopic calculations. Throughout much of the crust, the dominant neutrino emissivity is neutrino pair bremsstrahlung, $e^- + (A, Z) \rightarrow e^- + (A, Z) + \nu\bar{\nu}$ (Maxwell 1979; Haensel et al. 1996; Itoh et al. 1996). Where the ions are crystallized, the bremsstrahlung rates are exponentially suppressed because the separation between electron energy bands is of order 1 MeV $\gg k_B T$ (Pethick & Thorsson 1994, 1997). I use the fits of Haensel et al. (1996) for the emissivity where the ions are liquefied and the fits of Yakovlev & Kaminker (1996), which include this suppression, where the ions are crystallized. If the crust is very impure (see the discussion in § 3.3), then the crust bremsstrahlung will be dominated by electron-impurity scattering (Pethick & Thorsson 1997). For $T \gtrsim 10^9$ K and densities where $\hbar\omega_{pe}/k_B T \gtrsim 1$, $\hbar\omega_{pe} \approx 0.056(E_{F,e}/1 \text{ MeV}) \text{ MeV}$ being the electron plasma frequency, the plasma neutrino process (Schinder et al. 1987; Itoh et al. 1996) becomes important.

This paper assumes a standard core neutrino emissivity, for which modified Urca processes (Friman & Maxwell 1979; Yakovlev & Levenfish 1995) dominate. The phase space available for scattering is strongly restricted if the nucleons are superfluid and reduces the emissivity roughly as $\exp(-T/T_c)$ (Yakovlev & Levenfish 1995) where T_c is the superfluid transition temperature. In general, both the neutrons and protons must be superfluid to substantially reduce the modified

Urca neutrino luminosity. The proton modified Urca branch ($p + p \rightarrow p + n + e^+ + \nu_e$) is nearly as efficient as the neutron branch (Yakovlev & Levenfish 1995), and so a slight increase in temperature is sufficient to compensate for the suppression of just one of the modified Urca branches.

3.2. The superfluid transition temperatures

In the core, both the protons and neutrons are expected to be superfluid over some range of densities (Baym, Pethick, & Pines 1969; Hoffberg et al. 1970; Takatsuka & Tamagaki 1993; Amundsen & Østgaard 1985b; Amundsen & Østgaard 1985a; Elgarøy et al. 1996). At lower densities, the neutrons pair in a singlet (1S_0) state, but at higher densities the repulsive core of the interaction forces the neutrons to pair in a triplet (3P_2) state. The protons in the core are expected to be in a 1S_0 state. There is at present little agreement on the range of densities for which the protons and neutrons are superfluid and on their transition temperatures T_c (for a review, see Pethick et al. 1995). The early calculation of Hoffberg et al. (1970) for pure neutron matter found peak gap energies of 1.6 MeV (singlet) and ~ 5 MeV (triplet). They also found that the transition temperature remained high over a large range of densities, implying that the entire core would be superfluid. More recent calculations of the neutron triplet pairing (Takatsuka & Tamagaki 1993; Amundsen & Østgaard 1985b) find a lower transition temperature $k_B T_c^{\max} \lesssim 0.1$ MeV. In addition, the range of densities for which pairing occurs is restricted. Elgarøy et al. (1996), using a meson-exchange model for β -stable matter, found that maximum gap energy was ≈ 0.018 MeV and that the range of densities was restricted to $n \lesssim 0.13 \text{ fm}^{-3}$, so that almost all of the core would be normal. In all cases the proton pairing gaps are somewhat larger, with $k_B T_c^{\max} \sim 1.0$ MeV, and extend to densities several times the saturation density, $n_s = 0.16 \text{ fm}^{-3}$.

Although none of the published microscopic calculations of the critical temperature T_c has presented a convenient fitting formula in terms of density, the critical temperatures are roughly quadratic functions of the Fermi wavevector $k_{\{np\}} = (3\pi^2 n_{\{np\}})^{1/3}$. I therefore use

$$T_c(k) = T_{c0} \left[1 - \frac{(k - k_0)^2}{(\Delta_k/2)^2} \right] \quad (12)$$

as the functional form of T_c for the proton 1S_0 , neutron 1S_0 , and neutron 3P_2 states. The parameters T_{c0} , k_0 , and Δ_k are chosen (see Table 2) to approximate the transition temperature of Amundsen & Østgaard (1985b) for the neutron 3P_2 state and the transition temperature of Amundsen & Østgaard (1985a) for the proton and neutron singlet states. This choice of T_c reflects the calculations of Takatsuka & Tamagaki (1993) as well.

Figure 3 displays T_c for the proton 1S_0 (*solid lines*) and neutron 3P_2 (*dashed lines*) pairing as a function of density, for both equations of state. While the neutron critical temperatures are roughly identical, the proton critical temperature for AV18+ δv +UIX* vanishes at lower n . This cutoff is because AV18+ δv +UIX* has a higher proton fraction, at a given n , than AV14+UVII. For each EOS, I show (*arrows*) the central densities of neutron stars of gravitational masses $\mathcal{M} = 1.4M_\odot$.

Table 1. Hydrostatic structures

model	M (M_\odot)	\mathcal{M} (M_\odot)	R (km)	$1+z$	g ($10^{14} \text{ cm s}^{-2}$)	p_{crust} (MeV fm^{-3})	ΔM (M_\odot)
M1.4-14 ^a	1.58	1.4	10.7	1.28	2.08	0.60	0.025
M1.8-14 ^a	2.12	1.8	10.4	1.43	3.13		0.017
M1.4-18 ^b	1.56	1.4	11.6	1.25	1.74	0.39	0.021
M1.8-18 ^b	2.09	1.8	11.3	1.38	2.61		0.015

^aEOS is a fit (Lai 1994) to AV14+UVII (Wiringa et al. 1988)

^bEOS is AV18+ δv +UIX* (Akmal et al. 1998, appendix A)

Note. — M is the number of baryons in the star, multiplied by $m_n = 1.67 \times 10^{-24} \text{ g}$; \mathcal{M} is the gravitational mass of the star; p_{crust} is the pressure at the base of the crust; and ΔM is the number of baryons in the crust multiplied by m_n .

Table 2. Parameters used to calculate superfluid transition temperature (eq. [12]).

State	T_c (MeV)	k_0 (fm^{-1})	Δk (fm^{-1})
proton 1S_0	0.345	0.7	1.0
neutron 1S_0	0.802	0.7	1.2
neutron 3P_2	0.0776	2.0	1.6

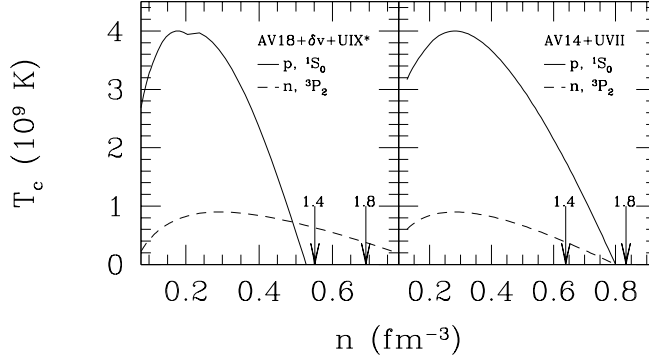


Fig. 3.— Superfluid transition temperature T_c (see eq. [12]) as a function of density, for both the proton 1S_0 (*solid lines*) and neutron 3P_2 (*dashed lines*) pairing. Each panel is for a different core EOS, as indicated in the legend. The arrows mark the central densities, for each EOS, of a neutron star of gravitational mass $\mathcal{M} = 1.4M_\odot$ and $\mathcal{M} = 1.8M_\odot$.

and $\mathcal{M} = 1.8M_\odot$. At core temperatures $\sim 5 \times 10^8$ K, each of the four EOS/mass combinations has normal protons, neutrons, or both in some part of the core. As a result, the modified Urca processes still play an important role in the neutron star’s thermal balance³.

3.3. Heat transport

Throughout the crust, relativistic electrons transport the heat. In the relaxation-time approximation, the conductivity is (e.g., Ziman 1972),

$$K = \frac{\pi^2}{3} k_B \frac{k_B T n_e}{m_e^*} \tau. \quad (13)$$

Here $m_e^* = E_{F,e}/c^2$ is the effective electron mass, and τ is the relaxation time. Where the ions are crystallized, $1/\tau = 1/\tau_{ee} + 1/\tau_{eQ} + 1/\tau_{ep}$, and where they are liquefied, $1/\tau = 1/\tau_{ee} + 1/\tau_{ei}$. In these formulae, τ_{ee} , τ_{eQ} , τ_{ep} , and τ_{ei} are respectively the relaxation times for electron-electron (Urpin & Yakovlev 1980; Potekhin, Chabrier, & Yakovlev 1997), electron-impurity (Itoh & Kohyama 1993), electron-phonon (Baiko & Yakovlev 1995), and electron-ion (Yakovlev & Urpin 1980) scattering. Electron-electron scattering is typically negligible over much of the crust because the strong degeneracy of the electrons restricts the available phase space.

³Recently, neutrino emission from the formation and destruction of Cooper pairs has received renewed interest (see Yakovlev, Kaminker, & Levenfish 1999, and references therein). For temperatures near the superfluid transition temperature, the neutrino emissivity is *enhanced* over that of modified Urca processes. I have not included this emissivity here; for an impure crust, this omission is not critical (see § 4.2).

The electron-impurity relaxation time is (Yakovlev & Urpin 1980)

$$\tau_{eQ} = \frac{p_F^2 v_F}{4\pi Q e^4 n_N} \Lambda_{eQ}^{-1}. \quad (14)$$

Here p_F and v_F are the momentum and velocity of an electron at the Fermi surface and $\Lambda_{eQ} \approx 2$ (Yakovlev & Urpin 1980) is the logarithmic Coulomb factor. The concentration of impurities enters through Q , which for a large number of ion species is (Itoh & Kohyama 1993)

$$Q \equiv \frac{1}{n_N} \sum_i n_i (Z_i - \langle Z \rangle)^2. \quad (15)$$

Here n_i and Z_i are the density and charge number of the i th species, $n_N = \sum_i n_i$ is the total ionic density, and $\langle Z \rangle = n_N^{-1} \sum_i n_i Z_i$ is the mean ionic charge number.

There are several contributions to the impurities in the crust. First, within each electron capture layer there are at least two species present. The electron capture from an even-even to an odd-odd nucleus is immediately followed by a second electron capture to a lower energy even-even nucleus (Haensel & Zdunik 1990b). Within each capture layer the impurity parameter is then $Q = 4n_Z n_{Z-2} / (n_Z + n_{Z-2})^2 \leq 1$, with n_Z and n_{Z-2} denoting the densities of the two species. Although Haensel & Zdunik (1990a,b) treated the electron captures as sharp transitions in the crust, in actuality the layers have a finite thickness set by competition between the flow timescale and the (weak) electron capture timescale (Bisnovaty-Kogan & Chechetkin 1979; Blaes et al. 1990; Bildsten & Cumming 1998). The zero-temperature electron capture rate is proportional to $(E_{F,e} - \delta)^3$, where δ is the reaction threshold. Where degenerate electrons supply the pressure, $E_{F,e}$ must increase with depth. The layers are thin in $E_{F,e}$, and because $p \propto E_{F,e}^4$, the layers are geometrically thin as well. For densities greater than neutron drip, however, the electrons no longer support the crust, and $E_{F,e}$ need not increase with depth. In fact, $E_{F,e}$ is actually less following an electron capture layer if the interface between layers of different composition is treated as a infinitely thin plane. The layers, although thin with respect to $E_{F,e}$, are then geometrically thick. In actuality, thermal broadening of the electron Fermi surface causes many of the captures to occur pre-threshold, and the capture layers are thickened to nearly the width between layers (Ushomirsky et al. 1999). Should the capture layers overlap, then Q in the mixed layer can become larger than unity.

The impurities manufactured within the capture layers are probably a small perturbation compared to those already present in the mixture entering the top of the crust. Schatz et al. (1999) found that $Q \sim 100$ immediately following the end of stable hydrogen burning. An accurate assessment of Q , throughout the crust, requires evolving the composition of an accreted fluid element on its journey through the crust. This task is beyond the scope of this initial survey, and I instead set upper and lower bounds on the conductivity. The upper bound to the conductivity is that of a pure crystal (electron-phonon scattering). To set the lower bound, first note that electron-impurity scattering dominates the conductivity wherever $\tau_{eQ} < \tau_{ep}$, with τ_{ep} being the

electron-phonon relaxation time (Baiko & Yakovlev 1995)

$$\tau_{ep} = \frac{\hbar}{\alpha k_B T} \Lambda_{ep}^{-1}. \quad (16)$$

Here α is the fine structure constant, and $\Lambda_{ep} \approx 13$ comes from integrating over the phonon spectrum. Equations (14) and (16) imply that for $Q \gtrsim 0.66(30 \text{ MeV}/E_{F,e})(Z/26)(k_B T/0.05 \text{ MeV})$ electron-impurity scattering determines the thermal conductivity in the crust. If the reactions in the crust do not significantly reduce Q from its large value at the base of the hydrogen/helium burning shell, then *the heat transport in the crust is controlled by electron-impurity scattering rather than electron-phonon scattering.*

If Q is very large ($\sim Z^2$), then the impurity relaxation time is roughly that of electron-ion scattering for a pure crystal (Yakovlev & Urpin 1980),

$$\tau_{ei} = \frac{p_F^2 v_F}{4\pi Z^2 e^4 n_N} \Lambda_{ei}^{-1}, \quad (17)$$

with $\Lambda_{ei} = \ln[(2\pi Z/3)^{1/3} \sqrt{1.5 + 3/\Gamma}] - 1$. Basically, the phonon spectrum is extremely disordered in this case. I therefore set a lower limit to the conductivity by using electron-ion scattering, i.e., by treating the ions as if they were liquefied. For consistency, I also use the liquid-state neutrino bremsstrahlung emissivity (Haensel et al. 1996) in conjunction with the electron-ion conductivity. The impurities in the crust reduce the conductivity but increase the neutrino emissivity.

In the core, heat is mostly carried by electrons, with neutrons contributing if they are normal (Flowers & Itoh 1979). I neglect here the neutron conductivity. This is a good approximation, as the core is practically isothermal (see § 4). In evaluating the electron-proton scattering terms, I used an effective proton mass $m_p^* = 0.7m_p$. The proton superfluidity both reduces the screening (increases the scattering) and reduces the proton scattering phase space (suppresses the scattering); I take these factors into account using the fits of Gnedin & Yakovlev (1995).

3.4. Boundary conditions and method of solution

The first boundary condition is simply $L|_{r=0} = 0$. For a fully self-consistent solution, the correct second boundary condition is a relation $L(T)|_{r=R}$, usually obtained from a separate photospheric calculation. This is unnecessary, however, when the hydrogen and helium burn steadily. The large energy release from this burning determines the temperature in the outer atmosphere, so that the temperature at the base of the hydrogen/helium burning shell is a function only of \dot{M} , \mathcal{M} , and R and may be calculated independently. In § 4, I show that the luminosity flowing outwards from the crust is in fact much smaller than that generated by the hydrogen/helium burning.

The second boundary condition, then, is $T|_{r=R} = T_\circ(\dot{m})$, where I take T_\circ from Schatz et al. (1999). Here \dot{m} is the accretion rate per unit area; the fiducial rate used by Schatz et al. (1999) is the Eddington rate appropriate for a Newtonian star of $\mathcal{M} = 1.4M_\odot$ and $R = 10 \text{ km}$ accreting a

solar composition plasma. Numerically, this rate is $\dot{m}_E = 8.8 \times 10^4 \text{ g cm}^{-2} \text{ s}^{-1}$ and is an excellent approximation to the lowest local accretion rate at which the hydrogen/helium burning is stable (see, e.g., Bildsten 1998). At $\dot{m} = \dot{m}_E$, the temperature at the base of the hydrogen/helium burning shell is $T_o = 5 \times 10^8 \text{ K}$. Although the Newtonian surface gravity used by Schatz et al. (1999) is less than the values used here, T_o is relatively insensitive to g ($T_o \propto g^{1/7}$; Bildsten 1998), so I do not adjust it for each model. This is not critical, as the thermal profile in the crust is insensitive to T_o (see § 4).

The accretion rate enters equations (9) and (10) through ϵ_N , which is scaled to the accretion luminosity L_A . Because T_o is only a function of \dot{m} , I use the same \dot{m} for each model; the luminosity from this accretion is then different for each EOS and mass. The global accretion rate, as measured by an observer infinitely far away, is (Ayasli & Joss 1982) $\dot{M} = 4\pi R^2 \dot{m}/(1+z)$, and the luminosity is

$$L_A = \frac{z}{1+z} \dot{M} c^2 = \frac{z}{(1+z)^2} 4\pi R^2 \dot{m} c^2. \quad (18)$$

For the fiducial local accretion rate \dot{m}_E , model M1.4-14 has $L_A = L_A^\circ = 1.95 \times 10^{38} \text{ erg s}^{-1}$; M1.8-14 has $L_A^\circ = 2.28 \times 10^{38} \text{ erg s}^{-1}$; M1.4-18, $2.12 \times 10^{38} \text{ erg s}^{-1}$; and M1.8-18, $2.51 \times 10^{38} \text{ erg s}^{-1}$. To solve the thermal structure, equations (9) and (10) are finite-differenced onto the mesh defined by the integration of equations (2)–(5). An initial guess is constructed by fixing the temperature throughout the star to T_o and integrating equation (9) from $L|_{r=0} = 0$. This trial guess is then iteratively refined by a relaxation technique (Press et al. 1992). The resolution of the mesh was tested by computing models with step fractions (see eq. [7]) $f = 0.05$ and $f = 0.02$.

4. Results

4.1. The influence of the microphysics on the thermal profile

As promised in section 3.3, I survey the uncertainties in the thermal conductivity by solving the thermal structure (eq. [9] and eq. [10]) with the conductivity alternately set by electron-phonon scattering and electron-ion scattering. Figure 4 shows the thermal profiles for these two cases with different degrees of superfluidity: strong (both neutrons and protons are superfluid with $T_c \gg T$ throughout the core; *top panel*), moderate (corresponding to the parameters in Table 2; *middle panel*), and nonexistent ($T_c = 0 \text{ K}$ for both neutrons and protons; *bottom panel*). The hydrostatic structure used in this plot is model M1.4-18 (see Table 1). I plot the proper temperature (i.e., the temperature a local thermometer would measure) because it controls the conductivity and neutrino emissivity.

The lower conductivity and enhanced bremsstrahlung from electron-ion scattering (*dotted lines*) produce a greater temperature variation throughout the crust than if the conductivity and bremsstrahlung were determined by electron-phonon scattering (*solid lines*). In the inner crust, the electron-phonon conductivity (Fig. 5, *solid line*) is an order of magnitude greater than the

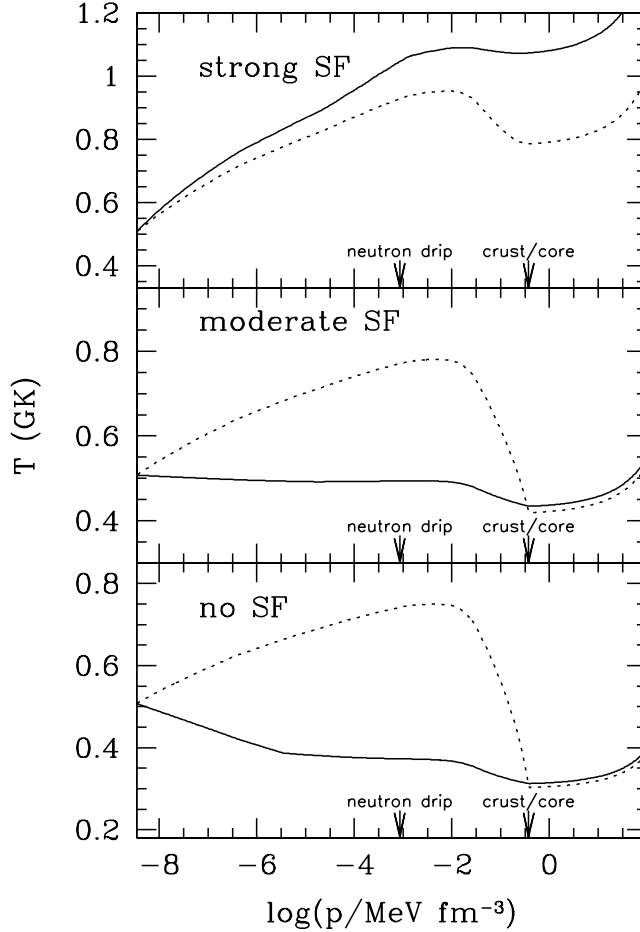


Fig. 4.— Proper temperature, in units of 10^9 K, as a function of pressure. The hydrostatic structure is M1.4-18 (see Table 1). Two cases are compared, with the conductivity dominated either by electron-phonon scattering (*solid lines*) or by electron-ion scattering (*dotted lines*). The three panels, from top to bottom, show the variation of the thermal profile with core superfluidity. In the top panel, the core neutrino emission is completely suppressed: both protons and neutrons are superfluid throughout the core. The middle panel shows the effects of moderate superfluidity (see Table 2), whereas in the bottom panel there is no superfluidity. Note that for a low thermal conductivity, the maximum crust temperature ($\approx 8 \times 10^8$ K) varies only slightly with the core temperature. The pressures of neutron drip and the crust-core boundary (see Table 1) are marked along the bottom axis of each plot with arrows.

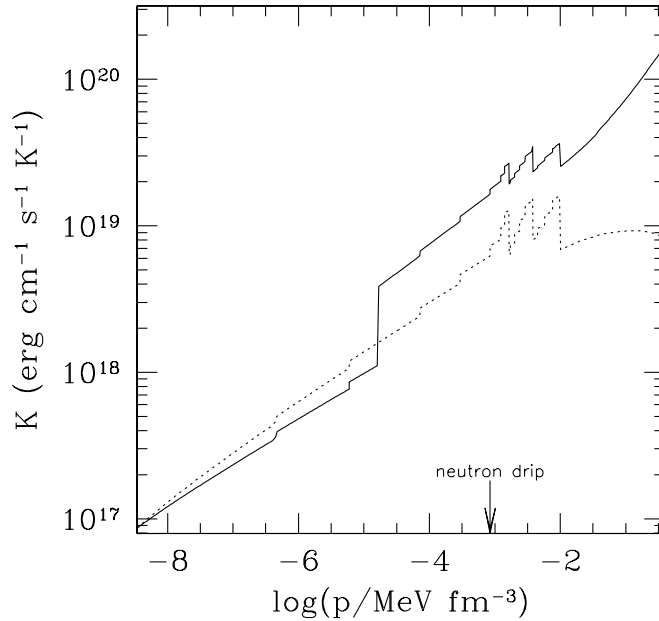


Fig. 5.— Thermal conductivity in the accreted crust. The thermal structure corresponds to the cases shown in the middle panel of Figure 4. Electron-phonon is denoted with a solid line, while electron-ion is denoted by a dotted line. Note that there is an order of magnitude difference between the two cases in the inner crust.

electron-ion conductivity (Fig. 5, *dotted line*). As a result, the thermal gradient in a locally pure crust is very small, so that the inner crust temperature is not appreciably different from that of the core. A striking result for this case is that the peak crust temperature depends only weakly on the core temperature. This is a consequence of the requirement that a large thermal gradient is needed to carry the flux in the inner crust when the conductivity is reduced.

The relative amounts of neutrino emission from the crust and core are displayed in Figure 6, which shows the luminosity measured by an observer at infinite distance and scaled to L_N . The lines and panels correspond to those of Figure 4, and for reference the region where nuclear heating occurs (see § 3.1) is denoted with boldfaced lines. A negative luminosity indicates that the heat flow is inward. When $T_c \gg T$ throughout the core for both neutrons and protons (*top panel*), all of the neutrinos are emitted from the crust, and the luminosity is zero throughout the core. For moderate superfluidity (Table 2; *middle panel*), some neutrino emission occurs in the crust when the conductivity and crust bremsstrahlung are dominated by electron-ion scattering (*dotted line*), but the bulk of the neutrinos are emitted in the innermost core, where the protons are normal. If there is no superfluidity, then neutrino emission occurs throughout the core (*bottom panel*). The decrease in L at pressures $\lesssim 10^{-3} \text{ MeV fm}^{-3}$ marks where the plasma neutrino emissivity dominates.

The core temperatures of the middle and bottom panels of Figure 4 are similar because the modified Urca emissivity is strongly temperature sensitive, so that the core temperature need only

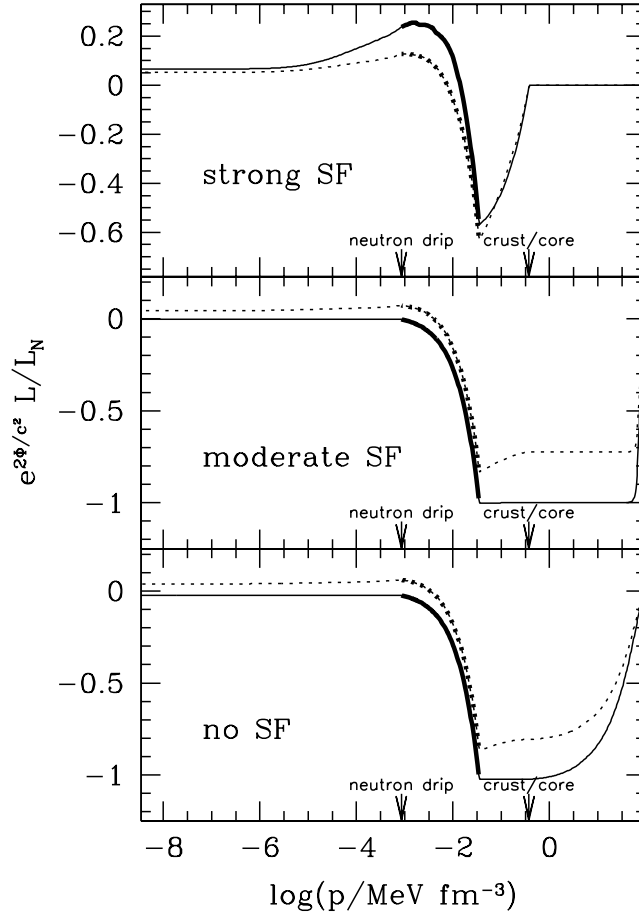


Fig. 6.— Luminosity, as measured by an infinitely distant observer and in units of the total crust nuclear luminosity L_N , plotted as a function of pressure. Negative values indicate an inwardly directed flux. The panels correspond to those in Figure 4, and both high conductivity (electron-phonon scattering; *solid lines*) and low conductivity (electron-ion scattering; *dotted lines*) cases are shown. The region where nuclear heating occurs is indicated with boldfaced lines.

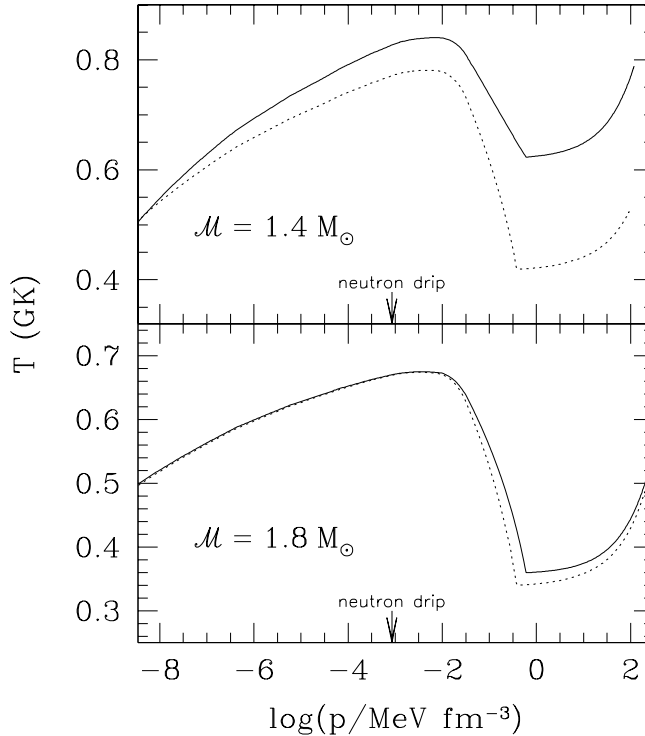


Fig. 7.— Proper temperature, in units of 10^9 K, as a function of pressure for two different core equations of state, AV14+UVII (*solid lines*) and AV18+ δv +UIX* (*dotted lines*), and two different gravitational masses, $\mathcal{M} = 1.4M_\odot$ (*top panel*) and $\mathcal{M} = 1.8M_\odot$ (*bottom panel*). The superfluidity is as described in Table 2, and the conductivity is set by electron-ion scattering throughout the crust. The pressures of the crust-core boundaries for the two EOS is given in Table 1.

slightly adjust to compensate for a reduced normal core fraction. To demonstrate this further, Figures 7 and 8 show, as functions of pressure, the proper temperatures and luminosities for the four models in Table 1 with conductivity set by electron-ion scattering. The equations of state AV14+UVII (*solid lines*) and AV18+ δv +UIX* (*dotted lines*) are compared for $\mathcal{M} = 1.4M_\odot$ (*top panel*) and $\mathcal{M} = 1.8M_\odot$ (*bottom panel*). For $\mathcal{M} = 1.8M_\odot$ the two equations of state have similar thermal profiles because both have normal protons and neutrons in at least some fraction of the core (see Figure 3). In contrast, for $\mathcal{M} = 1.4M_\odot$, only M1.4-18 (*top panel, dotted line*) has normal protons in its innermost core, and so its core temperature is quite cooler than that of M1.4-14 (*top panel, solid line*). As a result, M1.4-14 has a stronger neutrino emission from the crust (Figure 8, *top panel, solid line*). As in Figure 6, the nuclear heating region is denoted with boldfaced lines.

A generic feature of these solutions is that almost all of the nuclear heat released in the inner crust flows inward and is balanced by neutrino cooling from either the crust or core. Only a small amount ($\lesssim 5\%$) of L_N is conducted to the surface. As a result, the temperature in the inner crust and core is set by the processes in the inner crust. In particular, *the temperature of the*

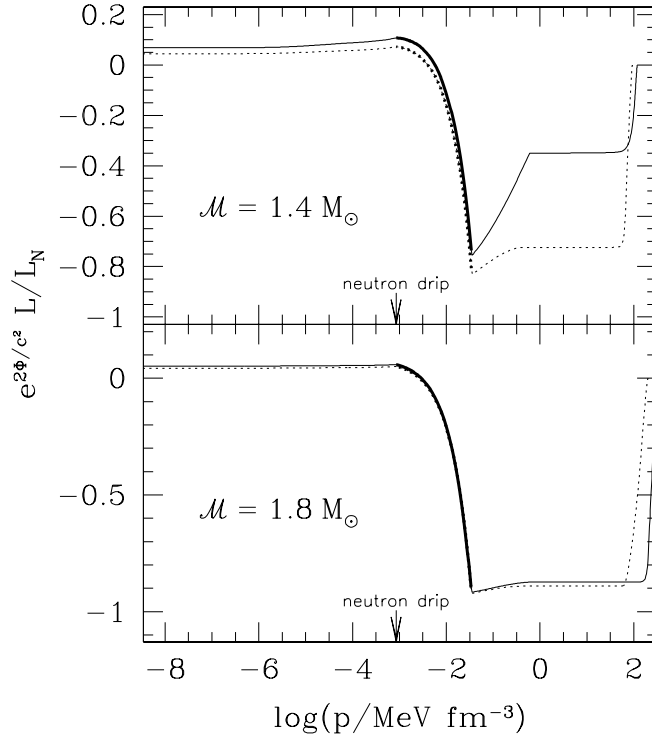


Fig. 8.— Luminosities corresponding to the thermal profiles in Fig. 7, with negative values indicating that the flux is inwardly directed. The higher neutrino emissivity from the modified Urca proton branch is evident for model M1.4-18 (*top panel, dotted line*): the AV18+ δv +UIX* EOS has a larger proton fraction Y_p and the protons in the inner portion of the core are normal (see Fig. 3). Nuclear heating occurs in the region denoted with boldfaced lines.

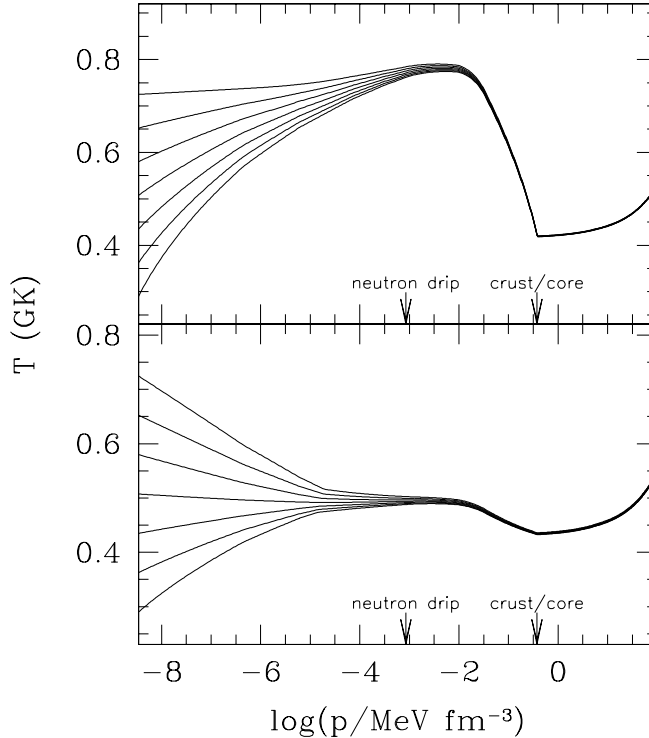


Fig. 9.— Proper temperature, in units of 10^9 K, as a function of pressure. A family of solutions for different T_0 , the temperature at the top of the crust, is shown, both for a thermal conductivity set by electron-ion scattering (*top panel*) and electron-phonon scattering (*bottom panel*). The temperature sensitivity of modified Urca processes (superfluidity as described in Table 2) keeps the base of the crust at a temperature $\approx 4.3 \times 10^8$ K in both cases.

inner crust is nearly independent of the temperature in the hydrogen/helium burning shell. This is explicitly shown in Figure 9, where I plot the thermal structure for model M1.4-18 but with the outer boundary temperature allowed to vary. The luminosity is fixed at $L_A^\circ = 2.12 \times 10^{38}$ erg s $^{-1}$. The top panel shows the case of electron-ion conductivity; the bottom, electron-phonon.

4.2. Analytical expressions for the crust temperature

The numerical results presented above can be easily understood by considering a crude analytical calculation of the thermal structure. The approach is similar to that of Hernquist & Applegate (1984), with three exceptions: I include heating from the crust reactions, I fit the pressure as a function of density, rather than presume a degenerate relativistic EOS, and I assume the conductivity is determined by electron-ion, rather than electron-phonon scattering.

In the crust, the surface gravity and radius are roughly constant, and the differential expressions

for the radius (eq. [2]), pressure (eq. [5]) and flux (eq. [10]) can be combined into the plane-parallel Newtonian equation

$$g\rho K \frac{dT}{dp} = \frac{L}{4\pi R^2}. \quad (19)$$

To construct this analytical model, I consider the heating and cooling emissivities to be δ -functions. Since the flux is then constant between points where these sources or sinks reside, I may integrate equation (19) piecewise between these points, with L stepping discontinuously at each point (Brown & Bildsten 1998).

Integrating equation (19) requires a relation $p(\rho)$. I approximate the mass density ρ by $m_u n$ and fit the pressure with power-laws in both the electron-dominated and neutron-dominated regions,

$$p = \begin{cases} 2.67 \times 10^{30} \rho_{12}^{1.27} \text{ dyne cm}^{-2}, & \rho_{12} \leq 0.66, \\ 4.97 \times 10^{29} \rho_{12}^{1.42} \text{ dyne cm}^{-2}, & \rho_{12} \geq 8.9. \end{cases} \quad (20)$$

Here $\rho_{12} = \rho/10^{12} \text{ g cm}^{-3}$, and the error in p is less than 9% and 5% for the two density regimes respectively⁴. The exponent in the electron-dominated regime is less than 4/3 because the fit accounts for the decrease in Y_e by electron captures. For densities just above neutron drip ($0.6607 < \rho_{12} < 8.913$), the pressure cannot be fit by a simple power-law in density (see Figure 2). This region is where most of the heat is released, and so for simplicity I presume the region to be isothermal and place the heating δ -function inside it.

Inserting the expression for the electron-ion scattering frequency (eq. [14]) into the expression for the thermal conductivity (eq. [13]) and expanding, I have

$$\begin{aligned} K &\approx \frac{1}{8} \left(\frac{\pi^5}{9}\right)^{1/3} \alpha^{-2} \hbar^{-1} \frac{Y_e^{1/3}}{Z} \left(\frac{\rho}{m_n}\right)^{1/3} k_B^2 T \\ &\approx 1.16 \times 10^{20} \left(\frac{Y_e^{1/3}}{Z}\right) \rho_{12}^{1/3} T_9 \text{ erg cm}^{-1} \text{ s}^{-1} \text{ K}^{-1}. \end{aligned} \quad (21)$$

In this expression, I set the Coulomb logarithm Λ_{ei} to unity and use the shorthand $T_9 = T/10^9 \text{ K}$. The composition enters through $Y_e^{1/3}/Z$; for densities less than neutron drip I use $Y_e^{1/3}/Z = 0.0298$, appropriate for a pure iron composition, and for densities greater than neutron drip I use $Y_e^{1/3}/Z = 0.0167$, as follows from the last entry of Table 2 in Haensel & Zdunik (1990b). (For impurity scattering, $Y_e^{1/3}/Z \rightarrow ZY_e^{1/3}/Q$.) Using equations (20) and (21), I integrate equation (19) from the top of the crust to neutron drip, $10^{-5} < \rho_{12} < 0.66$, and over the inner crust to the core, $8.913 < \rho_{12} < 166$, to obtain

$$T_9^2(\rho_{12}) = T_{\text{ND},9}^2 - 1.30 L_{o,35} R_{10}^{-2} g_{14.3}^{-1} (\rho_{12}^{-0.060} - 1.03) \quad (22)$$

for $\rho_{12} \leq 0.66$ and

$$T_9^2(\rho_{12}) = T_{\text{ND},9}^2 + 0.33 L_{i,35} R_{10}^{-2} g_{14.3}^{-1} (\rho_{12}^{0.087} - 1.21) \quad (23)$$

⁴In this section I use cgs units for easy comparison with the astrophysical literature.

for $\rho_{12} \geq 8.9$. In these equations T_{ND} is the temperature at neutron drip (presumed constant for $0.66 < \rho_{12} < 8.9$), $R_{10} = R/10$ km, $g_{14.3} = g/10^{14.3}$ cm s $^{-2}$, and $L_{o,35}$ and $L_{i,35}$ are the luminosities, in units of 10^{35} erg s $^{-1}$, for $\rho_{12} < 0.66$ and $\rho_{12} > 8.9$, respectively. Both L_o and L_i are signed: they are positive if the flux is directed outwards and negative if directed inwards. Notice that the coefficient of $L_{o,35}$ in equation (22) is an order of magnitude larger than the coefficient of $L_{i,35}$ in equation (23). This disparity reflects that the inner crust requires a much smaller thermal gradient than the outer crust to carry a given flux.

To solve for the thermal structure, I also require that the luminosity flowing away from the crust heat source is

$$L_N = L_o - L_i, \quad (24)$$

and that the core neutrino luminosity balances the heat conducted into the core,

$$L_i + L_\nu(T_{\text{core}}) = 0. \quad (25)$$

Evaluating equation (22) at $\rho_{12} = 10^{-5}$ and equation (23) at $\rho_{12} = 166$, and using equations (24) and (25) to replace L_o and L_i with L_N and L_ν , I obtain an equation for the core temperature,

$$T_{\text{core},9}^2 = T_{o,9}^2 + R_{10}^{-2} g_{14.3}^{-1} [1.26L_{N,35} - 1.38L_{\nu,35}(T_{\text{core},9})]. \quad (26)$$

Here $T_o = T|_{\rho_{12}=10^{-5}}$. Solving equation (26) for a modified Urca luminosity $L_{\nu,35} \approx 5 \times 10^4 T_{\text{core},9}^8$ and $L_N \approx 1.07 \times 10^{36}$ erg s $^{-1}$ (\dot{m}/\dot{m}_E) gives $T_{\text{core},9} = 0.34$ and $L_{\nu,35} = 0.92L_{N,35}$, i.e., 92% of the heat generated in the crust flows into the core. This compares reasonably well with the numerical calculation without core superfluidity (Figures 4 and 6, *bottom panels*). In that case, the proper temperature at the crust bottom is 3.1×10^8 K, the luminosity flowing out the top of the crust is $0.04L_N$, and the luminosity flowing into the core is $0.8L_N$. Neutrino emission from the crust balances the remainder of L_N .

Substituting $T_{\text{core},9}$ and $L_{\nu,35}$ into equation (23), I find that $T_{\text{ND},9} = 1.1$, which is an overestimation of the maximum crust temperature. This is a consequence of the “two-zone” treatment, which puts all of the neutrino cooling in the core. Still, the qualitative features of the numerical solutions are reproduced. In equation (23), the increase in temperature from core to neutron drip (second term, right-hand side) is much larger than $T_{\text{core},9}^2$. As a result, changing $T_{\text{core},9}$ has only a small effect on $T_{\text{ND},9}$. Even if the direct Urca process were to operate and cool the core to $T_{\text{core},9} \ll 1$, the temperature around neutron drip will remain high. *At high accretion rates, the temperature around neutron drip, for a very impure crust, is primarily determined by the ability of the inner crust to carry the nuclear luminosity inward and not so much by the efficiency of core neutrino cooling.*

4.3. Accretion at higher and lower rates

As the crust temperature increases, crust neutrino bremsstrahlung and the plasma neutrino process become increasingly important. At the higher accretion rate, the brighter crust neutrino

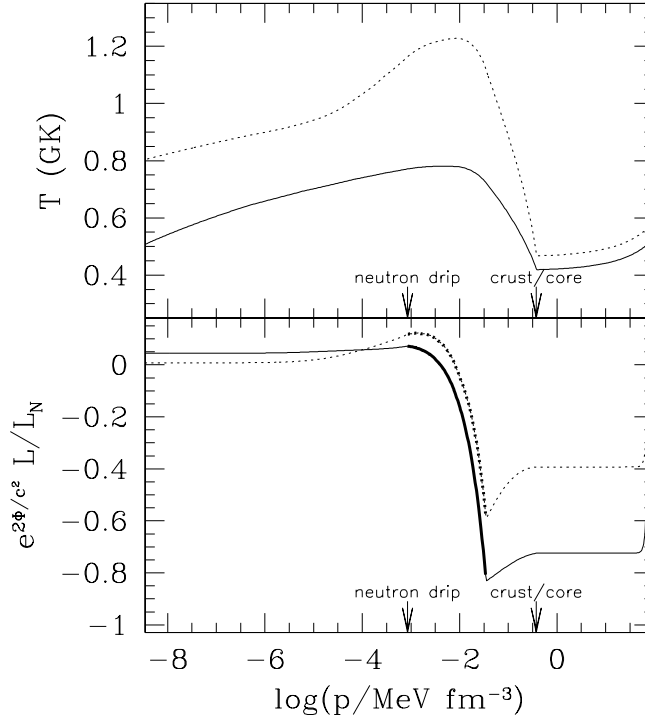


Fig. 10.— Proper temperature, in units of 10^9 K (*top panel*), and luminosity, scaled to the nuclear luminosity, as measured by an observer at infinity (*bottom panel*) for accretion luminosities $L_A^\circ = 2.12 \times 10^{38}$ erg s $^{-1}$ (*solid lines*) and $5L_A^\circ = 1.06 \times 10^{39}$ erg s $^{-1}$ (*dotted lines*). At the higher accretion rate, the cooling from crust bremsstrahlung and plasma neutrino emission balance the heating (*boldfaced lines*) on the spot, so that the luminosity flowing out the top of the crust is nearly zero.

luminosity balances the nuclear heating “on the spot.” Figure 10 compares proper temperature (*top panel*) and scaled luminosity (*bottom panel*), as measured by an observer at infinite distance, for model M1.4-18 accreting at \dot{m}_E ($L_A = L_A^\circ = 2.12 \times 10^{38}$ erg s $^{-1}$; *solid line*) and $5\dot{m}_E$ ($L_A = 5L_A^\circ = 1.06 \times 10^{39}$ erg s $^{-1}$; *dotted line*). The conductivity in both cases is set by electron-ion scattering. As the crust neutrino cooling increases, a smaller fraction of L_N flows outward from the top of the crust.

At lower accretion rates, the change in temperature over the inner crust becomes smaller relative to the core temperature. The crust becomes more nearly isothermal and hence more sensitive to the temperatures at its boundaries (cf. Miralda-Escudé et al. 1990; Zdenik et al. 1992). From equation (23), the temperature increase over the inner crust is $< 0.5T_{\text{core}}$ for $L_A < 0.06L_A^\circ$, assuming that $L_i = L_N$. To demonstrate this, Figure 11 displays, for an accretion luminosity $L_A = 0.01L_A^\circ = 2.12 \times 10^{36}$ erg s $^{-1}$, the proper temperature and luminosity. The hydrostatic structure is M1.4-18, the same as in Figure 9. The top panel is for a conductivity set by electron-ion scattering; the bottom panel is for a conductivity set by electron-phonon scattering. Solutions for several T_\circ

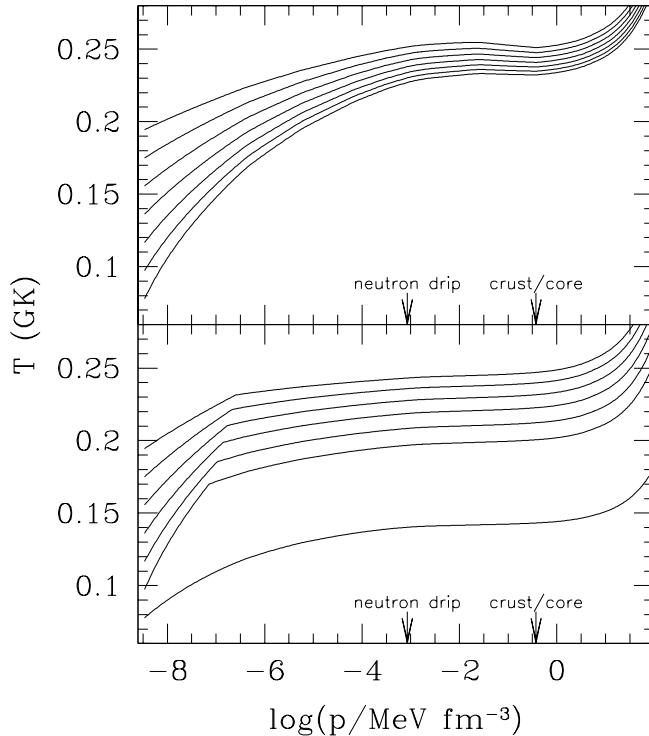


Fig. 11.— Temperature, in units of 10^9 K, as a function of pressure for an accretion luminosity 1/100 of the fiducial rate plotted in Fig. 9. Both the high-conductivity (electron-phonon scattering; *bottom panels*) and low-conductivity (electron-ion scattering; *top panels*) cases are considered. Unlike Fig. 9, the temperature in the inner crust and core depends more on the temperature at the top of the crust. The sharp kink in the thermal profiles (*bottom panel*) is where the ions crystallize.

are shown; the range of values are reduced from those used in Figure 9 by $(\dot{m}/\dot{m}_E)^{2/7} = 0.01^{2/7}$, which is roughly how the temperature at the base of a hydrogen/helium burning shell scales with accretion rate (Schatz et al. 1999). Of course, the hydrogen and helium ignition is unstable in an envelope this cold (see Bildsten 1998, and references therein), and so T_\circ is determined by the compression of matter in the atmosphere and by the flux flowing out the top of the crust. As T_\circ is reduced, more and more of the heat generated in the crust flows outwards rather than into the core. As found by Zdunik et al. (1992), an enhanced core neutrino emissivity will drastically lower the crust temperature for low accretion rates.

To illustrate how the crust temperature changes with the temperature in the hydrogen/helium burning region (T_\circ), I compute the derivative $dT_{\text{crust}}/dT_\circ$, where T_{crust} is the temperature at the centroid of the heat-producing region, $p = 0.017 \text{ MeV fm}^{-3}$. Figure 12 displays $dT_{\text{crust}}/dT_\circ$ as a function of T_\circ for five different accretion rates: $L_A/L_A^\circ = 0.01$ (*hollow triangles*), 0.03 (*filled triangles*), 0.1 (*hollow squares*), 0.3 (*filled squares*), and 1.0 (*asterisks*). When the conductivity is low (electron-ion scattering; *top panel*), T_{crust} is generally less sensitive to T_\circ than when electron-

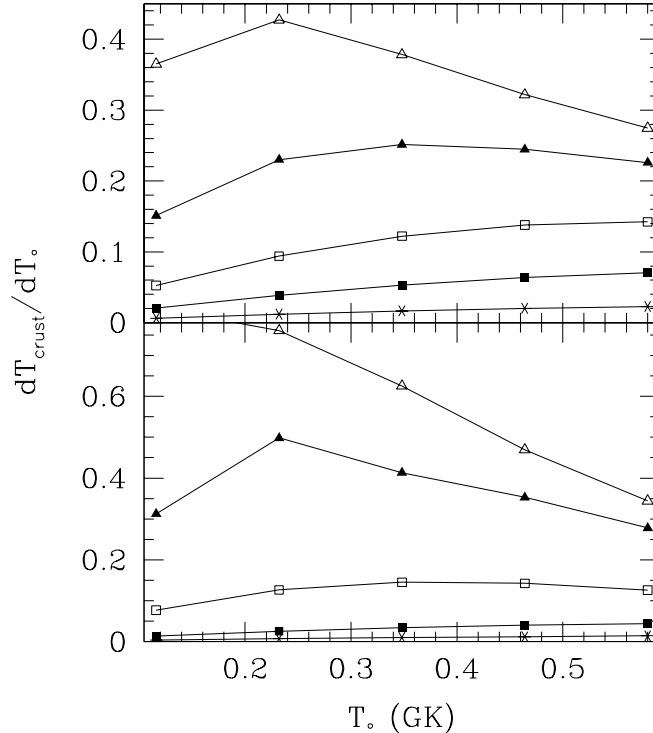


Fig. 12.— Derivative of the crust temperature (at the centroid of the heat-producing region, $p = 0.017 \text{ MeV fm}^{-3}$) with respect to the temperature at the top of the crust (in units of 10^9 K) for $L_A/L_A^\circ = 0.01$ (*hollow triangles*), 0.03 (*filled triangles*), 0.1 (*hollow squares*), 0.3 (*filled squares*), and 1.0 (*asterisks*). The top panel is for a low conductivity (electron-ion scattering) crust, while the bottom is for a high conductivity (electron-phonon scattering) crust.

phonon scattering sets the heat transport (*bottom panel*). The derivative (at a given accretion rate) is largest when $T_0 = T_{\text{crust}}$; this peak is evident in the top panel for $L_A/L_A^\circ = 0.01$ and in the bottom panel for $L_A/L_A^\circ = 0.03$. The rapid rise of dT_{crust}/dT_0 in the bottom panel for $L_A/L_A^\circ = 0.01$ is because the neutrino cooling in the crust and core goes to zero, so that all of the heat generated in the crust flows outwards (cf. Figure 11, *bottom panel*). In addition, the crust in the entire region considered is also crystalline, which reduces dT/dp . In general, for $\dot{M} \gtrsim 10^{-9} M_\odot/\text{yr}^{-1}$, the temperature in the crust becomes independent of the temperature in the atmosphere and upper ocean of the neutron star.

4.4. Crust melting

An interesting possibility for a rapidly accreting neutron star is that its crust may melt. This happens wherever $\Gamma \lesssim 170$, where the exact value is uncertain (for a review, see Ichimaru 1982).

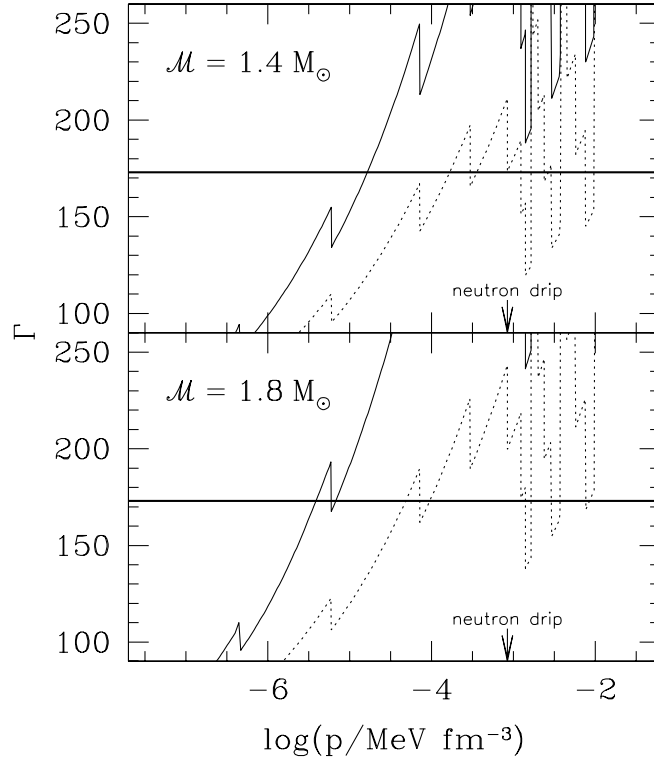


Fig. 13.— Ion coupling parameter Γ as a function of pressure in the neutron star crust, for M1.4-18 (*top panel*) and M1.8-18 (*bottom panel*), as described in Table 1. The conductivity is alternately dominated by electron-phonon scattering (*solid lines*) and electron-ion scattering (*dotted lines*). I also display the melting criterion $\Gamma = 173$ (*heavy solid lines*).

Since I use the formulation of Farouki & Hamaguchi (1993) to calculate the ionic free energy, I also adopt their melting value, $\Gamma_M = 173$. The crust reactions reduce Z and heat the crust; both of these effects decrease Γ , as shown in Figure 13 for models M1.4-18 (*top panel*) and M1.8-18 (*bottom panel*), with each model accreting at its fiducial rate. In both cases, the core superfluidity is as described in Table 2. For a low thermal conductivity (*dotted lines*), the crust melts in a series of layers. The jaggedness of Γ is because of the pycnonuclear reactions. Each one doubles Z and halves n_N , so that Γ increases by $2^{5/3}$ and the crust refreezes. Electron captures then decrease Z and Γ until the crust melts again.

As a consequence of this melting and freezing, the crust resembles a layer cake at densities greater than neutron drip. Figure 14 shows the nuclear charge Z_M (*thin line*), below which the ions are liquid, along with the Z of the nuclei present (*thick lines*) according to Haensel & Zdunik (1990a). The thermal structure is the same as plotted in Figure 13, top panel, dotted line. Γ increases with density (or equivalently, Z_M decreases), and so the naive expectation is a sharp transition from an ionic ocean to a crust. The Fermi energy also increases with density, however,

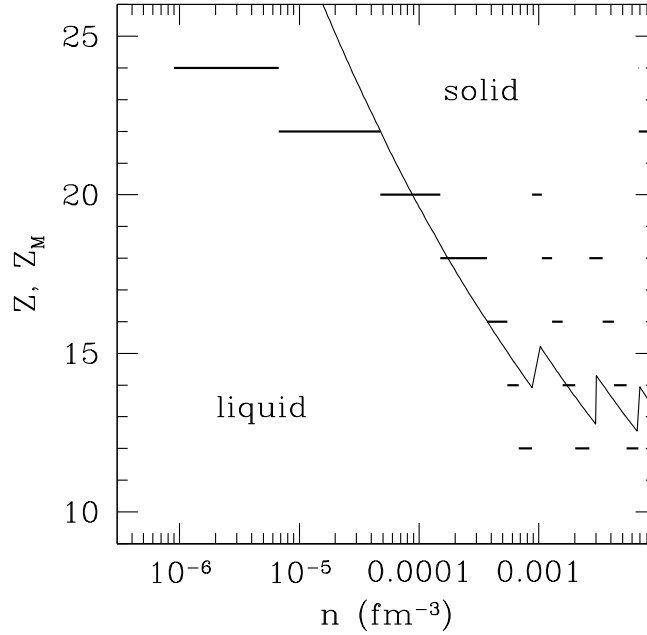


Fig. 14.— Nuclear charge Z_M (*thin solid line*) such that a pure lattice composed of ions of charge $Z < Z_M$ melts, as a function of density n . This solution is for the same parameters as Fig. 13, top panel, dotted line. The ions are liquid in the region below this curve and crystalline in the region above it. Also plotted are the Z of the nuclei present at each depth (*heavy lines*), according to Haensel & Zdunik (1990a).

and the ensuing decrease in Z from electron captures offsets the rise in Γ : both Z_M and Z decrease together. The melting strongly depends on composition: an increment of Z by 2–3 is enough to keep the crust crystalline throughout.

Notice from Figure 13 that there is no crustal melting if the conductivity is solely determined by electron-phonon scattering, for models M1.4-18 and M1.8-18 (*solid lines*). For model M1.4-14, the crust melts even if the conductivity is set by electron-phonon scattering. For larger masses (models M1.8-14 and M1.8-18), a high impurity concentration is needed to ensure melting. This is a consequence of the stronger core neutrino cooling holding the crust at a slightly lower temperature (cf. Figures 7 and 8). Of course, when the impurity concentration is high, the single-species calculation of Γ (eq. [6]) is no longer applicable. Calculations for binary-ionic mixtures (e.g., Segretain & Chabrier 1993) show that the melting temperature is lowered below that of the pure phases. While the phase diagram of a plasma composed of a large number of species has not been calculated, it is likely that the Γ_M of an impure crust is lower than that assumed here. This strengthens the contention that the impure crust of a rapidly accreting neutron star contains melted layers, provided that the Z used here (from Haensel & Zdunik 1990a) is roughly the average charge of the nuclei actually present. A self-consistent calculation of the crust composition, and the

resulting phase diagram, is required to conclusively determine if layer cake melting actually occurs.

5. Summary and concluding remarks

There are three main conclusions presented in this work. First, for neutron stars accreting rapidly enough for the accreted hydrogen and helium to burn stably, most of the heat released in the crust flows into the core. As a result, the thermal profile in the inner crust is nearly independent of the temperature at the top of the crust. Second, if the crust lattice is very impure, there is a maximum in temperature at densities greater than neutron drip, where the heating occurs. The peak temperature in the crust in this case is set by the ability of the crust to carry the generated nuclear luminosity inward from the reaction shell and is relatively insensitive to the core temperature. Third, heating the inner crust to temperatures $\approx 8 \times 10^8$ K might melt the crust in thin layers where electron captures have reduced the ionic charge.

There are several consequences of these results. Because a fluid layer does not support shear stress, the strain in the crust must vanish in these melt layers. This will limit the quadrupole that can be induced by thermal perturbations to the electron capture rate (Bildsten 1998) if these captures occur above the melt layer. In addition, the fluid layers can dissipate rotational energy, either through hydrodynamical or magnetohydrodynamical processes, and thus contribute to balancing the accretion torque acting on the stellar surface. The electrical conductivity of an accreted crust is reduced, both because of crust heating (Urpin & Geppert 1995; Geppert & Urpin 1994) and because of crust impurities (Brown & Bildsten 1998). If the crust is as impure as considered here, the timescale for Ohmic decay over a pressure scaleheight is much less (by a factor of 100) than the flow timescale, for much of the crust. As a result, the inward advection of magnetic flux (Konar & Bhattacharya 1997) is reduced in importance. Thermomagnetic effects, such as current drift (Geppert & Urpin 1994) and the battery effect (e.g., Blandford, Applegate, & Hernquist 1983), will be comparatively more important, however, because of the greater thermal gradient.

In recent years, attention has been given to other, more efficient, cooling mechanisms. The direct Urca process can operate if the proton fraction is greater than 0.148 (Lattimer et al. 1991) or if hyperons are present (Prakash et al. 1992). Other exotic mechanisms may be possible, including pion condensates (Umeda et al. 1994), kaon condensates (Brown et al. 1988), or quark matter (Iwamoto 1982). The exotic mechanisms have the same temperature dependence as the direct Urca ($\propto T^6$) but are weaker. Although none of the hydrostatic structures considered in this paper has an interior proton fraction large enough to activate the direct Urca, some form of enhanced cooling could operate. However, the crust temperature would still remain high (§ 4.2) if the crust were very impure. Direct observational consequences of the core neutrino emissivity are unfortunately lacking. It is only in the cooling after accretion halts and the crust thermally relaxes (as in the transients; Brown, Bildsten, & Rutledge 1998) that the mode of core neutrino emissivity can be investigated. This is unlike the case of isolated, cooling neutron stars, for which the core neutrino cooling must be treated correctly.

The results of this investigation show that the most vexing impediment to further calculations of the thermal structure of an accreting neutron star, and hence to a better understanding of the issues raised in this section, is the need to calculate the composition throughout the crust for the trajectory in (n, T) space followed by an accreted fluid element.

It is a pleasure to thank Lars Bildsten, Andrew Cumming, Andrew Melatos, and Greg Ushomirsky for many helpful discussions and for reading drafts of this work. I also thank Chris Pethick for suggesting that the nuclei in the inner crust may remain spherical if the charge is low enough and the referee for helpful comments on the melting of a multi-species crystal. This research was supported by NASA grant NAG5-8658. EFB is supported by a NASA GSRP Graduate Fellowship under grant NGT5-50052.

REFERENCES

- Akmal, A., Pandharipande, V. R., & Ravenhall, D. G. 1998, *Phys. Rev. C*, 58, 1804
- Amundsen, L. & Østgaard, E. 1985a, *Nucl. Phys. A*, 437, 487
- . 1985b, *Nucl. Phys. A*, 442, 163
- Andersson, N. 1998, *ApJ*, 502, 708
- Andersson, N., Kokkotas, K. D., & Schutz, B. F. 1999, *ApJ*, 510, 846
- Andersson, N., Kokkotas, K. D., & Stergioulas, N. 1999, *ApJ*, 516, 307
- Ayasli, S. & Joss, P. C. 1982, *ApJ*, 256, 637
- Baiko, D. A. & Yakovlev, D. G. 1995, *Astr. Letters*, 21, 702
- Baym, G., Pethick, C., & Pines, D. 1969, *Nature*, 224, 673
- Bhattacharya, D. 1995, in *X-ray Binaries*, ed. W. H. G. Lewin, J. van Paradijs, & R. E. Taam (Cambridge University Press), 233–251
- Bildsten, L. 1998, *ApJ*, 501, L89
- Bildsten, L. 1998, in *The many faces of neutron stars*, ed. A. Alpar, R. Buccheri, & J. van Paradijs, NATO/ASI (Dordrecht: Kluwer)
- Bildsten, L. & Cumming, A. 1998, *ApJ*, 506, 842
- Bildsten, L., Salpeter, E. E., & Wasserman, I. 1992, *ApJ*, 384, 143
- Bisnovatyi-Kogan, G. S. & Chechetkin, V. M. 1979, *Soviet Physics Uspekhi*, 127, 263

- Blaes, O., Blandford, R., Madau, P., & Koonin, S. 1990, *ApJ*, 363, 612
- Blaes, O. M., Blandford, R. D., Madau, P., & Yan, L. 1992, *ApJ*, 399, 634
- Blandford, R. D., Applegate, J. H., & Hernquist, L. 1983, *MNRAS*, 204, 1025
- Brown, E. F. & Bildsten, L. 1998, *ApJ*, 496, 915
- Brown, E. F., Bildsten, L., & Rutledge, R. E. 1998, *ApJ*, 504, L95
- Brown, G., Kubodera, K., Page, D., & Pizzochero, P. 1988, *Phys. Rev. D*, 37, 2042
- Champagne, A. E. & Wiescher, M. 1992, *Ann. Rev. Nucl. Part. Sci.*, 42, 39
- Elgarøy, Ø., Engvik, L., Hjorth-Jensen, M., & Osnes, E. 1996, *Phys. Rev. Lett.*, 77, 1428
- Farouki, R. & Hamaguchi, S. 1993, *Phys. Rev. E*, 47, 4330
- Flowers, E. & Itoh, N. 1979, *ApJ*, 230, 847
- Friedman, J. L. & Morsink, S. M. 1998, *ApJ*, 502, 714
- Friman, B. L. & Maxwell, O. V. 1979, *ApJ*, 232, 541
- Fujimoto, M. Y., Hanawa, T., Iben, I., & Richardson, M. B. 1984, *ApJ*, 278, 813
- Fujimoto, M. Y. & Sugimoto, D. 1982, *ApJ*, 257, 291
- Geppert, U. & Urpin, V. 1994, *MNRAS*, 271, 490
- Gnedin, O. Y. & Yakovlev, D. G. 1995, *Nucl. Phys. A*, 582, 697
- Haensel, P., Kaminker, A. D., & Yakovlev, D. G. 1996, *A&A*, 314, 328
- Haensel, P. & Zdunik, J. L. 1990a, *A&A*, 229, 117
- . 1990b, *A&A*, 227, 431
- Hanawa, T. & Fujimoto, M. Y. 1984, *PASJ*, 36, 199
- Hernquist, L. & Applegate, J. H. 1984, *ApJ*, 287, 244
- Hoffberg, M., Glassgold, A. E., Richardson, R. W., & Ruderman, M. 1970, *Phys. Rev. Lett.*, 24, 775
- Ichimaru, S. 1982, *Rev. Mod. Phys.*, 54, 1017
- Itoh, N., Hayashi, H., Nishikawa, A., & Kohyama, Y. 1996, *ApJS*, 102, 411
- Itoh, N. & Kohyama, Y. 1993, *ApJ*, 404, 268

- Iwamoto, N. 1982, *Ann. Phys.*, 141, 1
- Koike, O., Hashimoto, M., Arai, K., & Wanajo, S. 1999, *A&A*, 342, 464
- Konar, S. & Bhattacharya, D. 1997, *MNRAS*, 284, 311
- Lai, D. 1994, *MNRAS*, 270, 611
- Lamb, D. Q. & Lamb, F. K. 1978, *ApJ*, 220, 291
- Landau, L. D. & Lifshitz, E. M. 1980, *Course of theoretical physics, Vol. 5, Statistical Physics, part 1*, 3rd edn. (Oxford: Pergamon Press)
- Lattimer, J. M., Pethick, C. J., Prakash, M., & Haensel, P. 1991, *Phys. Rev. Lett.*, 66, 2701
- Lindblom, L., Owen, B. J., & Morsink, S. M. 1998, *Phys. Rev. Lett.*, 80, 4843
- Lorenz, C. P., Ravenhall, D. G., & Pethick, C. J. 1993, *Phys. Rev. Lett.*, 70, 379
- Mackie, F. D. & Baym, G. 1977, *Nucl. Phys. A*, 285, 332
- Maxwell, O. V. 1979, *ApJ*, 231, 201
- Miralda-Escudé, J., Paczynski, B., & Haensel, P. 1990, *ApJ*, 362, 572
- Misner, C. W., Thorne, K. S., & Wheeler, J. A. 1973, *Gravitation* (New York: W. H. Freeman and Company)
- Negele, J. W. & Vautherin, D. 1973, *Nucl. Phys. A*, 207, 298
- Owen, B. J., Lindblom, L., Cutler, C., Schutz, B. F., Vecchio, A., & Andersson, N. 1998, *Phys. Rev. D*, 58, 084020
- Oyamatsu, K. 1993, *Nucl. Phys. A*, 561, 431
- Paczyński, B. 1983, *ApJ*, 267, 315
- Pethick, C. J. & Ravenhall, D. G. 1995, *Annu. Rev. Nucl. Part. Sci.*, 45, 429
- Pethick, C. J. & Ravenhall, D. G. 1998, in *Trends in nuclear physics, 100 years later*, ed. H. e. a. Nifenecker, *Les Houches Sesion LXVI, 1996* (New York: Elsevier)
- Pethick, C. J., Ravenhall, D. G., & Lorenz, C. P. 1995, *Nucl. Phys. A*, 584, 675
- Pethick, C. J. & Thorsson, V. 1994, *Phys. Rev. Lett.*, 72, 1964
- . 1997, *Phys. Rev. D*, 56, 7548
- Potekhin, A. Y., Chabrier, G., & Yakovlev, D. G. 1997, *A&A*, 323, 415

- Prakash, M., Prakash, M., Lattimer, J. M., & Pethick, C. J. 1992, *ApJ*, 390, L77
- Press, W. H., Teukolsky, S. A., Vetterling, W. T., & Flannery, B. P. 1992, *Numerical Recipes in FORTRAN* (Cambridge: Cambridge University Press)
- Romani, R. W. 1990, *Nature*, 347, 741
- Salpeter, E. E. & van Horn, H. M. 1969, *ApJ*, 155, 183
- Sato, K. 1979, *Prog. Theor. Physics*, 62, 957
- Schatz, H., Arahamian, A., Goerres, J., Wiescher, M., et al. 1998, *Phys. Rep.*, 294, 167
- Schatz, H., Bildsten, L., Cumming, A., & Wiescher, M. 1999, *ApJ*, in press. Preprint available: astro-ph/9905274
- Schinder, P. J., Schramm, D. N., Wiita, P. J., Margolis, S. H., & Tubbs, D. L. 1987, *ApJ*, 313, 531
- Segretain, L. & Chabrier, G. 1993, *A&A*, 271, L13
- Takatsuka, T. & Tamagaki, R. 1993, *Prog. Theor. Phys. Supp.*, 112, 27
- Thorne, K. S. 1977, *ApJ*, 212, 825
- Tsuruta, S. 1998, *Phys. Rep.*, 292, 1
- Umeda, H., Nomoto, K., Tsuruta, S., Muto, T., & Tatsumi, T. 1994, *ApJ*, 431, 309
- Urpin, V. & Geppert, U. 1995, *MNRAS*, 275, 1117
- Urpin, V., Geppert, U., & Konenkov, D. 1998, *A&A*, 331, 244
- Urpin, V. A. & Yakovlev, D. G. 1980, *Soviet Ast.*, 24, 126
- Ushomirsky, G., Cutler, C., & Bildsten, L. 1999, *ApJ*, in preparation
- van der Klis, M. 1998, in *The many faces of neutron stars*, ed. A. Alpar, R. Buccheri, & J. van Paradijs, NATO/ASI (Dordrecht: Kluwer)
- van Riper, K. A. 1991, *ApJS*, 75, 449
- Van Wormer, L., Gorres, J., Iliadis, C., Wiescher, M., et al. 1994, *ApJ*, 432, 326
- Wallace, R. K. & Woosley, S. E. 1981, *ApJS*, 45, 389
- Webbink, R. F., Rappaport, S., & Savonije, G. J. 1983, *ApJ*, 270, 678
- Wiringa, R. B., Fiks, V., & Fabrocini, A. 1988, *Phys. Rev. C*, 38, 1010
- Yakovlev, D. G. & Kaminker, A. D. 1996, *Astr. Letters*, 22, 491

Yakovlev, D. G., Kaminker, A. D., & Levenfish, K. P. 1999, *A&A*, 343, 650

Yakovlev, D. G. & Levenfish, K. P. 1995, *A&A*, 297, 717

Yakovlev, D. G. & Urpin, V. A. 1980, *Soviet Ast.*, 24, 303

Zdunik, J. L., Haensel, P., Paczynski, B., & Miralda-Escude, J. 1992, *ApJ*, 384, 129

Ziman, J. M. 1972, *Principles of the theory of solids*, 2nd edn. (Cambridge: Cambridge University Press)